Electron Energization by Turbulent Electric Fields: A Possible Source of the Outer Radiation Belt

[1]M.E. Usanova and [1,2]R.E. Ergun

[1]Laboratory for Atmospheric and Space Physics, University of Colorado, Boulder, Colorado, USA

[2]Department of Astrophysical and Planetary Sciences, University of Colorado, Boulder, Colorado, USA

Abstract

The turbulent energy cascade that is characteristic of bursty bulk flow (BBF) braking regions in the Earth's magnetotail has been shown to be the energy source for large-amplitude electric fields (>50 mV/m) which can, in turn, result in local energetic electron acceleration. These pre-energized electrons move inward to stronger magnetic fields being adiabatically energized and can eventually supply an energetic tail to electron distributions in the outer radiation belt. Using wave and plasma measurements from the Time History of Events and Macroscale Interactions during Substorms (THEMIS) satellites during four tail seasons from 2015 to 2019, we study the process of BBF magnetic and kinetic energy being transferred to electrons by turbulent electric fields from a statistical perspective. We identify turbulent BBF regions by the presence of high-amplitude electric fields. We show that the high-amplitude electric fields are associated with an increase in electron temperature by three times compared to quiet times and with a ten-fold increase in temperature fluctuations. They are also associated with strong variations of energetic electron fluxes, indicative of local acceleration. We further discuss the implications of these findings and the role of this pre-energized electron population in supplying the outer radiation belt.

Main point #1. Large-amplitude electric fields are associated with ten-fold electron temperature fluctuations and energetic electron flux variations.

Main point #2. Temperature and flux variations rather than absolute temperature and flux values are indicative of local acceleration.

Main point #3. The accelerated electrons may serve as a seed population for the high-energy tail of the outer radiation belt.

1. Introduction

Bursty bulk flows (BBFs) are high-speed plasma flow events, observed in Earth's plasma sheet (Baumjohann et al., 1990; Angelopoulos et al., 1992). They are believed to be generated by magnetic reconnection in the tail at distances greater than about ~20-30 Earth radii (Re) (Chen and Wolf, 1993). Earthward BBFs observed in the plasma sheet within a wide range of geocentric distances from 5 to 30 Re are characterized by dipolarization (an increase in the B_z magnetic field component) and a decrease in plasma density and plasma pressure (Ohtani et al., 2004). BBFs are spatially localized in the direction of the flow and are often confined to <3 Re in the dawn-dusk direction (Angelopoulos et al., 1997). Due to their localization, these events are most often observed as bursts ~10 min duration. Between 10 and 20 Re their speeds reach several hundred to over a thousand km/s in earthward direction. As BBFs move closer to Earth (6-12 Re tailward), they slow down and deflect as their energy dissipates (Shiokawa et al., 1997). The region over which the flow is slowed and diverted in the near-Earth tail is known as the BBF braking region.

The flow braking can generate turbulent plasma fluctuations and instabilities (e.g., Shiokawa et al., 2005; El-Alaoui et al., 2013). These fluctuations can exhibit properties of MHD- and kinetic scale Alfvén waves being involved in a turbulent cascade in BBFs (Chaston et al., 2012, 2014; Stawarz et al., 2015). The energy cascade has also been found associated with tail reconnection (Dai et al., 2011; Ergun et al., 2020) and observed in the plasma sheet boundary layer between 4 and 6 Re (Wygant et al., 2002).

Ergun et al. (2015) found that BBF braking events can be accompanied by high-amplitude electric fields (>50 mV/m). The large-amplitude electric fields have been observed at radial distances between 10 and 13 Re (Sigsbee et al., 2002) and as far in as 6 Re (Nishimura et al. 2008; Chaston et al., 2014), consistent with the BBF braking

location. These large-amplitude electric field events share a number of characteristics such as enhanced magnetic field fluctuations, magnetic field dipolarization, fluctuating ion flow velocities, ion and electron heating, and strong, field-aligned Poynting flux which might be responsible for the generation of Alfvénic aurora (Dubyagin et al., 2010; Nakamura et al., 2014). A significant portion of electric field spectral power density typical to these events is above the ion cyclotron frequency. It often contains nonlinear Debye scale structures, also known as time domain structures, i.e., double layers and electron phase space holes (Ergun et al., 2009; 2015). The spectra of low-frequency electric and magnetic field fluctuations also found to exhibit power law behavior that may be indicative of turbulence. Stawarz et al. (2015) hypothesized that Alfvénic turbulence is generated in the BBF braking region at the expense of the free energy in the BBF. Small-scale Alfvén waves (e.g., Lysak et al., 2009) or Alfvénic turbulence (e.g., Karimabadi et al., 2013) can drive strong, localized, currents and electron beams which may provide the source for the observed large-amplitude electric fields (Kindel and Kennel, 1971; Newman et al., 2001; Ergun et al., 2005). In addition, strong turbulence may produce the necessary conditions for the development of a significant nonthermal tail in both the electron and ion distributions (Ergun et al., 2020). The turbulence cascades the driving energy to smaller scales and higher frequencies at which electrons can efficiently absorb energy. Turbulence also generates magnetic depletions that trap the particles and impart unequal dwell times, causing relatively few particles to absorb a disproportionately large amount of energy.

BBFs contribute a large fraction of the observed mass, energy, and magnetic flux transport towards Earth in the magnetotail (Baumjohann et al., 1990; Angelopoulos et al., 1994). Even though these flows are sporadic, they can have a significant impact on the energetic particle dynamics in the magnetosphere. Transient dipolarizations within BBFs (also known as dipolarization fronts) are often accompanied by dispersionless particle injections - simultaneous sudden particle flux enhancements at energies of tens to hundreds keV (e.g., Gabrielse et al., 2012; 2014; Liu et al., 2016) - indicative of local acceleration process. Injections play an important role in the inner magnetosphere dynamics by providing a source population (10 - 300 keV ions and electrons) for the ring

current and outer radiation belt. Deep injections can supply even higher energy electrons, up to a few MeV as observed inside geosynchronous orbit by Dai et al. (2015).

The relative importance of large-scale electric and magnetic fields in the acceleration and transport of injected particles is still debatable. Numerically, this problem is usually studied by test-particle simulations of electron and ion trajectories in the dipolarization electric and magnetic fields in the magnetotail. Originally, the energization was suggested to be associated with ExB drift in the inductive electric field due to betatron (conserving the first adiabatic invariant) and Fermi acceleration (conserving the second adiabatic invariant) or a combination thereof (e.g., Williams et al., 1990). Later, non-adiabatic effects have became the focus of attention. For example, Delcourt (2002) demonstrated that the nonadiabatic ion behavior can lead to significant local acceleration, mainly in the direction perpendicular to the background magnetic field. Since particles with larger Larmor radii are unmagnetized more easily, they are much more susceptible to energization by a local electric field.

Recent test particle simulations in high-resolution MHD fields have shown that depolarization fronts can provide conditions for magnetic trapping and further particle energization even in the absence of large electric fields (Ukhorskiy et al., 2017, 2018; Sorathia et al., 2018). However due to their intrinsic global nature, the MHD models are not suitable to simulate local wave-particle interactions and have a limiting factor in accurately reproducing the highest-energy outer belt electron fluxes. Therefore, to model kinetic effects and study their role in the dynamics of the magnetotail three-dimensional global kinetic simulations are warranted.

In this paper, we expand on the Ergun et al. (2015) study and investigate the relationship between the observed turbulent electric fields and electron energization in BBFs. In Section 2, we describe THEMIS orbits and instrumentation used for this study. In Section 3, we present an event example showing the relationship between the strong electric fields and electron heating. In Section 4, we describe the automated event detection algorithm and BBF selection criteria. In Section 5, we examine the relationship between the electric field amplitudes and electron temperature and energetic flux fluctuations. In

Section 6, we discuss the role of pre-energized electron population in supplying the outer radiation belt. Section 7 concludes our study.

2. Instrumentation

The Time History of Events and Macroscale Interactions during Substorms (THEMIS) is a mission originally employing five identical spacecraft launched on February 17, 2007 (Angelopoulos, 2008). In December 2009, THEMIS B and C were sent to the Moon, while the remaining three probes continued orbiting the Earth at ~10-15 Re apogee, THEMIS D being on the highest elliptical orbit. The probes carry instrumentation to measure electric and magnetic fields as well as charged particles at several time resolutions. For this study, we use data from Electric Field Instrument (EFI) (Bonnell et al., 2008; Cully et al., 2008), Fluxgate Magnetometer (FGM) (Auster et al., 2008), electrostatic analyzer (ESA) electron measurements in the a few eV up to 30 keV energy range (McFadden et al., 2008), and Solid State Telescopes (SST) electron differential energy flux within the energy range from 41 to 203.5 keV (Angelopoulos et al., 2008). We surveyed a total of 1038 days of data from probes A, D and E during the tail seasons of 2015-2019.

3. Observations

An example of event of interest is shown in Figure 1. The event was observed on THEMIS A at 08:26-08:28 and 08:45-08:57 UT on March 5, 2018. Panel a) shows enhancements in the SST omnidirectional electron differential energy flux from six energy channels spanning 41 to 203.5 keV. These enhancements are also seen in the ESA omnidirectional electron differential energy flux from six energy channels between 9 and 32 keV in Panel b). In addition, SST flux variations and ESA temperature fluctuations were calculated by removing a continuous, linear trend over a 100 s interval. SST electron differential energy flux variations in the 139 keV channel are shown in Panel c). ESA electron temperature (black) and temperature fluctuations (red) are plotted in Panel d). Panels e) and f) show an on-board computed electric field spectrogram and filterbank (FBK) electric field root mean square (RMS) amplitude of the 144 and 572 Hz frequency bins, respectively. Electric field peaks selected with an automated algorithm (discussed in section below) applied to the FBK data are shown by the red crosses. Electric field components in burst

mode, Bx, By, Bz, and |B| magnetic field, and ion Vx, Vy, Vz velocity components are shown in Panels g), h) and i). The electric and magnetic time series and ion velocities are plotted in GSM coordinates.

Overall, the events are characterized by the presence of strong, up to ~100 mV/m, electric fields, fluctuations in magnetic field and ion velocity, and electron heating and acceleration. The intervals where they are observed are shaded by the grey bars. Remarkably, the strong electric fields are well correlated with variations in electron fluxes over a wide range of energy, covering both ESA and SST measurements. We argue that these variations indicate a local acceleration process.

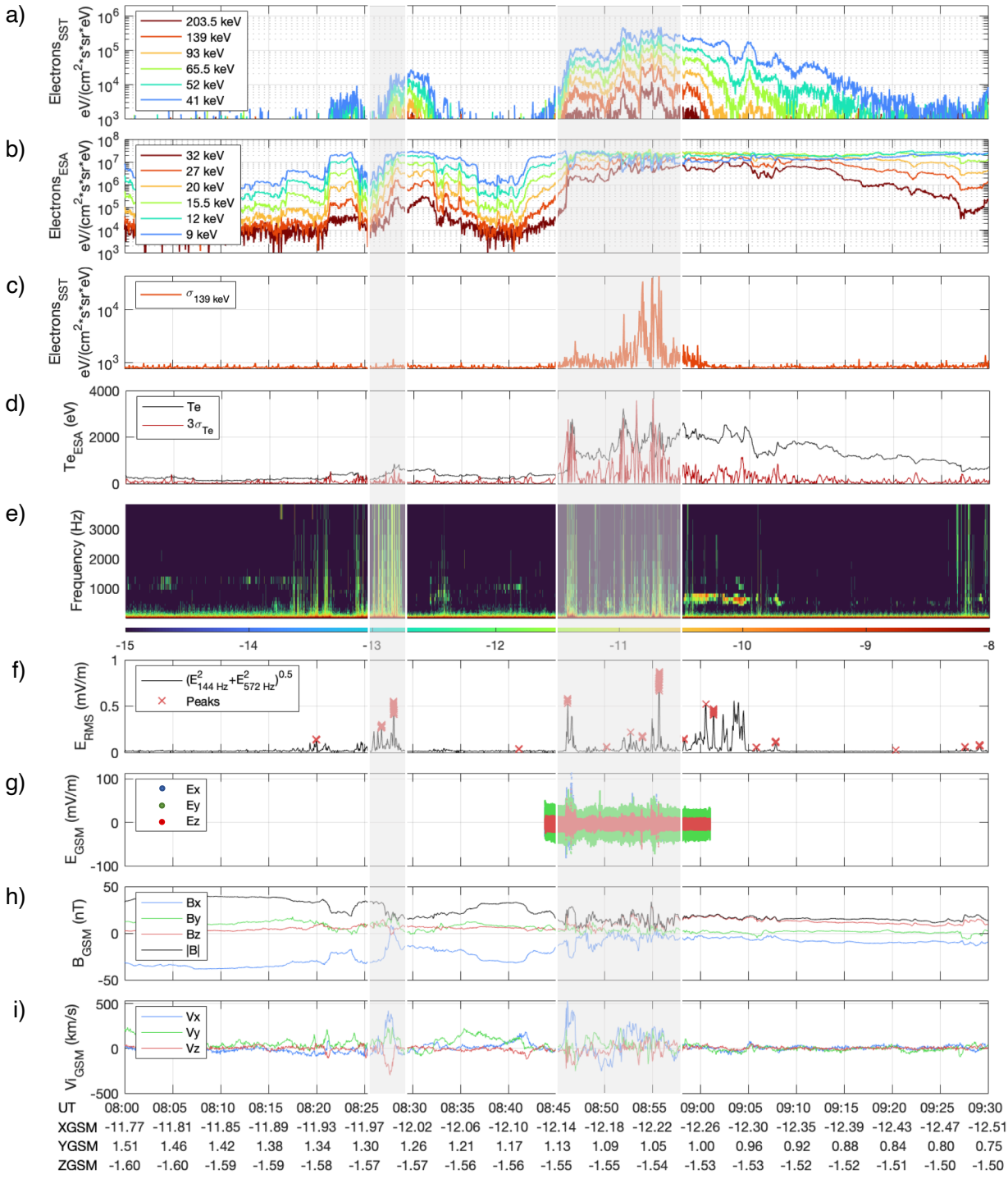

Figure 1. Summary plot of an event example from THEMIS A at 08:26-08:28 and 08:45-08:57 UT on March 5, 2018. a) SST omnidirectional electron differential energy flux in the 41, 52, 65.5, 93, 139 and 203.5 keV energy channels; b) ESA omnidirectional electron differential energy flux in the 9, 12, 15.5, 20, 27 and 32 keV energy channels; c) SST

electron differential energy flux variations in the 139 keV energy channel; d) ESA electron temperature (black) and temperature fluctuations (red); e) electric field spectrogram; f) on-board computed FBK electric field RMS amplitude averaged between the 144 and 572 Hz channels (black) and selected peaks (red); g) EFI Ex, Ey, Ez electric field components in burst mode; h) FGM Bx, By, Bz , |B| magnetic field; i) ESA ion Vx, Vy, Vz velocity components. The electric and magnetic time series and ion velocities are plotted in GSM coordinates (x: blue, y: green, and z: red curves). The magnetic field magnitude is plotted in black.

4. Automated Event Detection Algorithm and BBF Selection Criteria

In this section, we describe the event search criteria. First, we identify intervals of strong electric fields. For this, we select electric field peaks from the onboard computed electric field RMS amplitude recorded by the filterbank. The advantage of using FBK is that it provides continues coverage, as opposed to the sporadic burst intervals where high-cadence electric field time series are recorded. Filterbank data contain RMS amplitudes in multiple frequency channels, from 2.2 to 2689 Hz (Cully et al., 2008). The average between the second, 144 Hz and the third, 572 Hz channels is used as these channels were found to be least contaminated by other wave modes, e.g., chorus, hiss and ultra-low-frequency waves. After checking and removing data spikes, we compute a moving average and standard deviation within a 30-minute window and subtract the moving average from the signal. We select all the points exceeding three standard deviations, further referred to as peaks. Overall, we have analyzed 25,698,639 FBK data points and identified 317,416 peaks. The remaining 25,381,223 data points are referred to as non-peaks.

Strong electric fields are not specific to bursty bulk flows and can naturally occur in various regions of the magnetosphere, for example, they can be associated with inner magnetospheric plasma wave modes, e.g., time-domain structures (TDS; e.g., Mozer et al., 2013; 2015). In this study, we focus on electron energization in BBFs, hence we set additional criteria to select BBF events: magnetic field fluctuations, |dB| must exceed 5 nT and the maximum ion speed within a $\pm$30 second interval around the identified electric field peak must be greater than 100 km/s. These additional selection criteria were used

for the statistical analysis presented below. In addition, we set two different thresholds for the minimum electric field amplitude, >0.1 mV/m and >1 mV/m to examine the relationship between electric field amplitude and electron heating. Figure 2 shows the distribution of 6528 peaks with amplitude >0.1 mV/m peaks (left) and 25,381,223 non-peaks (right) on a scatter plot in the GSM coordinates (the Sun is on the left). The color indicates ESA electron temperature. Overall, the spatial distribution of events is consistent with Ergun et al. (2015). Most events are located at Re=5-15, consistent with the BBF braking region. The duskside prevalence is in line with reported occurrences of BBFs (e.g., Raj et al., 2002). Similar dawn-dusk occurrence rate asymmetry was seen in the magnetotail for both depolarizing flux bundles and injections (Liu et al., 2013; 2016; Gabrielse et al., 2014), likely caused by asymmetric tail reconnection (Nagai et al., 2013). The large number of events just inside of 12 Re is due to the spacecraft dwell time at their apogee. To eliminate this bias, we binned the data on the XY_{GSM}-grid at 0.5 Re resolution and plotted the event occurrence distribution normalized by the spacecraft dwell time in Figure 3.

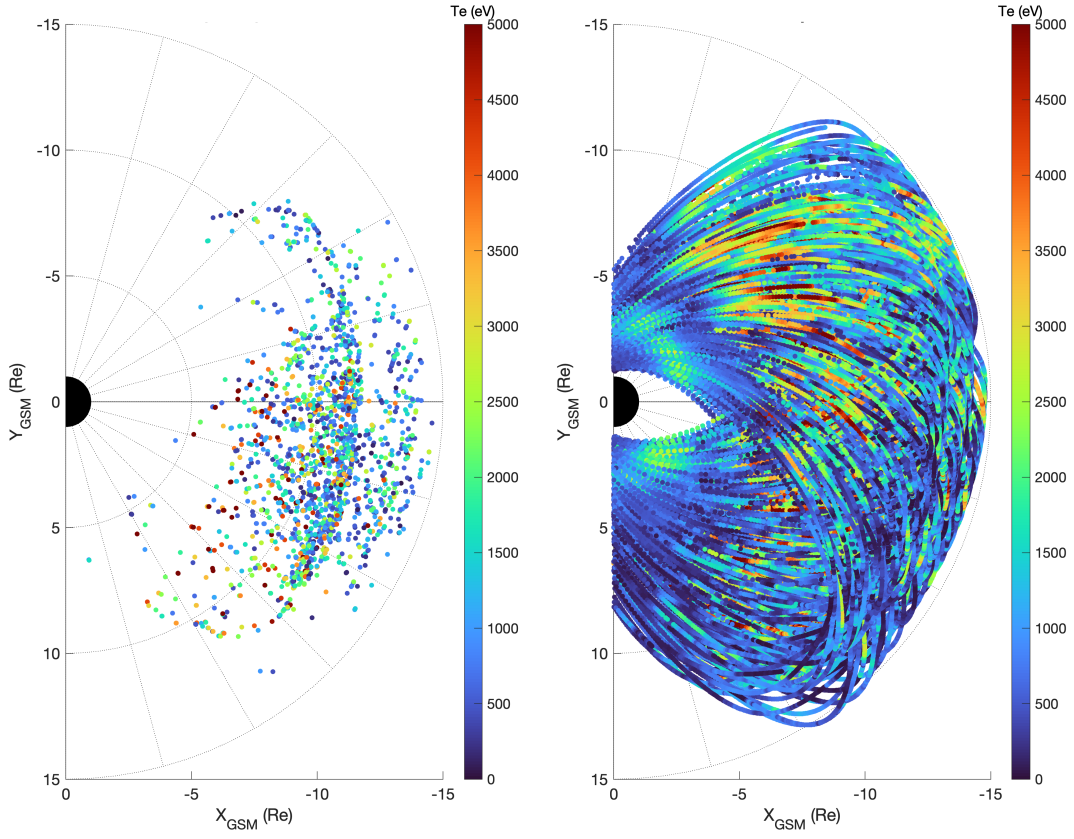

Figure 2. Scatter plot of >0.1 mV/m peaks (left) and non-peaks (right). Color represents the ESA electron temperature.

The diagrams in Figure 3 show the number of >0.1 mV/m peaks (left), non-peaks (center), and peaks' % occurrence (right). The occurrence rate of peaks is uniform and relatively low, ~0.1% demonstrating the transient nature of these events.

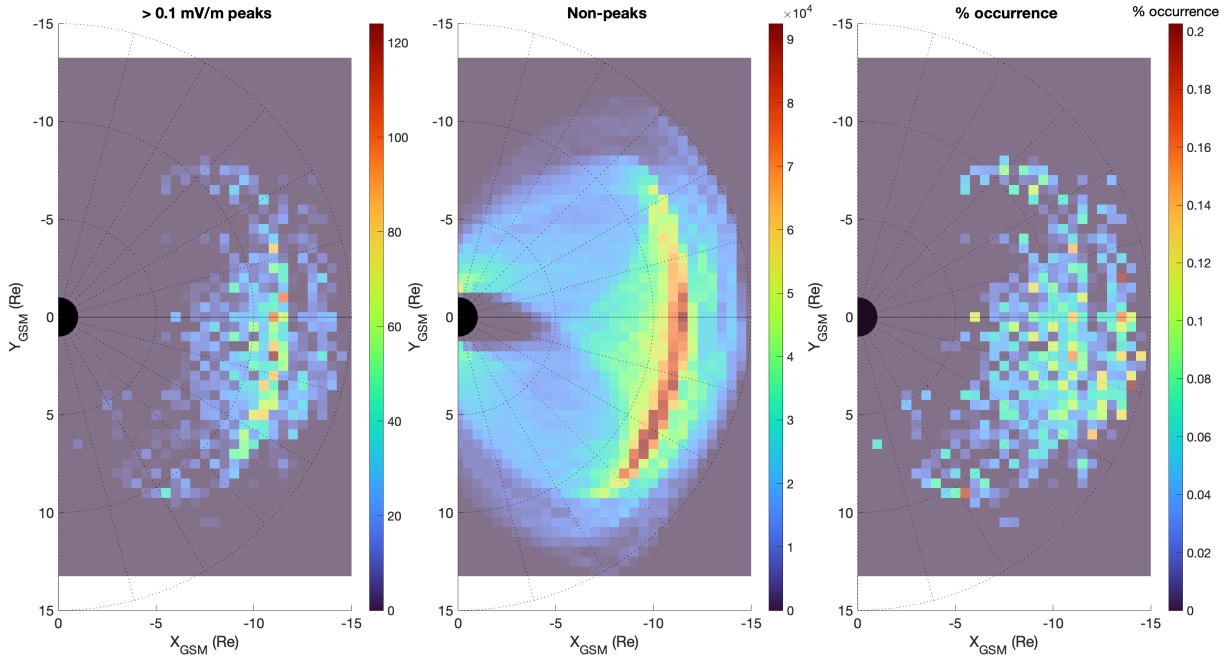

Figure 3. Diagrams showing the number of >0.1 mV/m peaks (left), non-peaks (center), and peaks' % occurrence (right).

Figure 4 shows electron temperature for >0.1 mV/m peaks (left) and non-peaks (center). The percent difference between the peaks' and non-peaks' temperature, $\frac{Te_{peaks}-Te_{non-peaks}}{Te_{peaks}} \cdot 100\%$ is shown in the right panel. The temperature distribution is different for peaks and non-peaks. For peaks, it maximizes at ~5 keV in the dusk sector, ~19-21 MLT and radial distances from 5 to 10 Re, and gradually decreases towards dawn. For non-peaks, the trend is opposite: the maximum temperature, ~3 keV is observed near dawn. The latter dawn-dusk asymmetry is consistent with previous THEMIS observations of electron temperature that attributed the asymmetry to the eastward electron drift and simultaneous adiabatic energization (e.g., Wang et al., 2012; Dubyagin et al., 2016; Ma et al., 2020). This contrast between the peaks' and non-peaks' trends results in the

percent difference being positive (~300-400%) in the dusk sector and negative (~-100%) in the dawn sector. A similar distribution is observed for >1 mV/m peaks (not shown here).

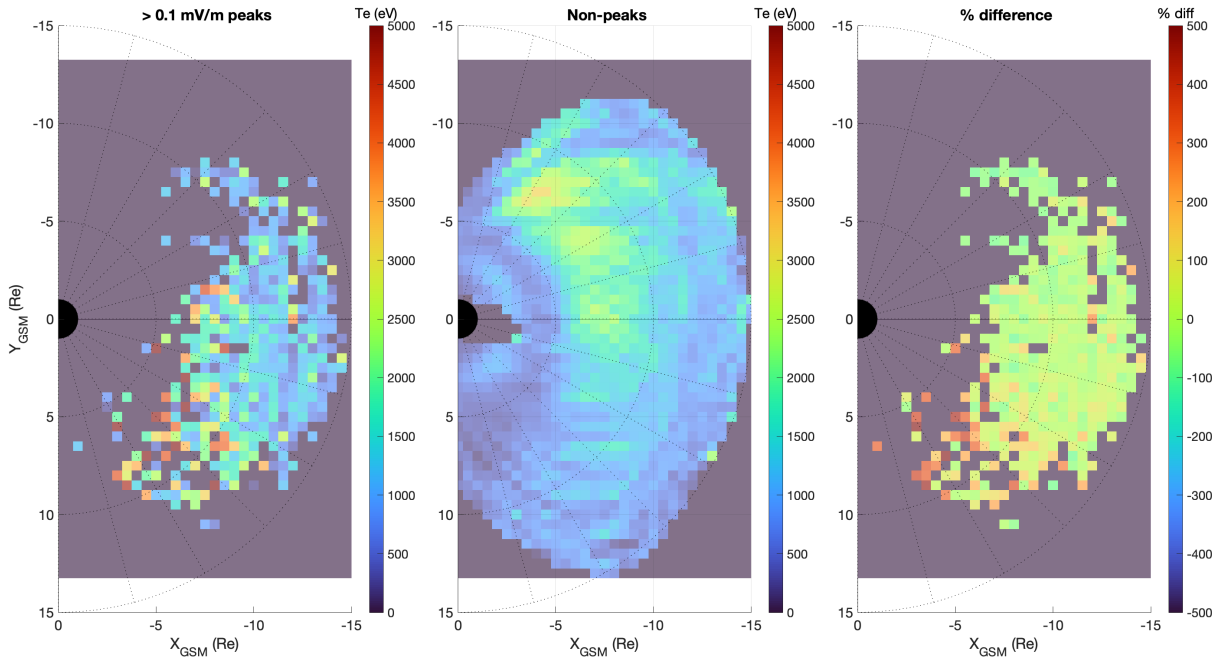

Figure 4. ESA electron temperature for >0.1 mV/m peaks (left) and non-peaks (center). The percent difference between the peaks' and non-peaks' temperature (right).

5. Electric Field Amplitude and Electron Temperature and Energetic Flux Variations

Here we discuss a relationship between the electric field amplitude and fluctuations in electron temperature and energetic electron fluxes. The ESA temperature is representative of core population while SST measurements depict the behavior of more energetic electrons at the tail of electron distribution. The left-hand panels of Figures 5 and 6 show electron temperature fluctuations for two electric field RMS thresholds, >0.1 mV/m and >1 mV/m, respectively. The center panels show electron temperature fluctuations for non-peaks, and the right-hand panels show a percent difference between the peaks and non-peaks, $\frac{|\sigma_{Te_{peaks}}|-|\sigma_{Te_{non-peaks}}|}{|\sigma_{Te_{peaks}}|} \cdot 100\%$. The temperature fluctuations reach their maximum, ~±1 keV for peaks; especially in the dusk sector. The fluctuations also increase for non-peaks in the morning sector, however they are generally less pronounced. The difference between the peaks and non-peaks is positive, up to ~1000% as shown in the right-hand side panels.

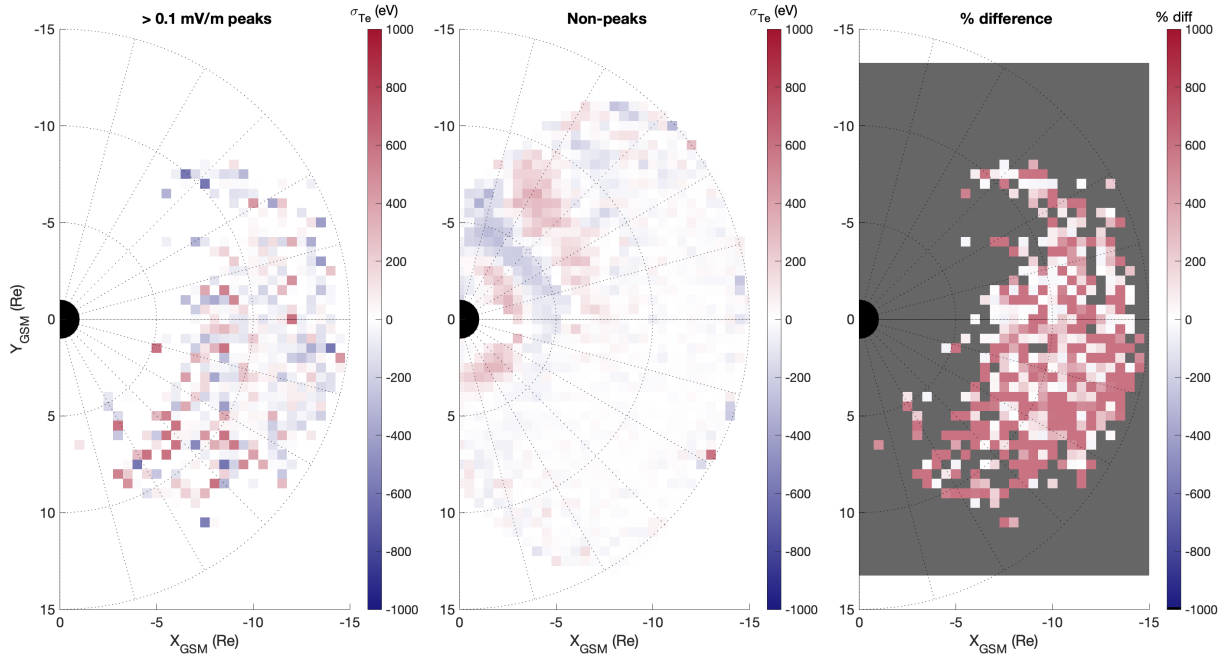

Figure 5. Electron temperature fluctuations for >0.1 mV/m peaks (left), non-peaks (center) and % difference between the peaks and non-peaks (right).

The difference becomes even more distinct for high-amplitude, >1 mV/m peaks, where it often approaches or even exceeds 1000% as demonstrated in Figure 6. This indicates that the temperature fluctuations increase with electric field amplitude.

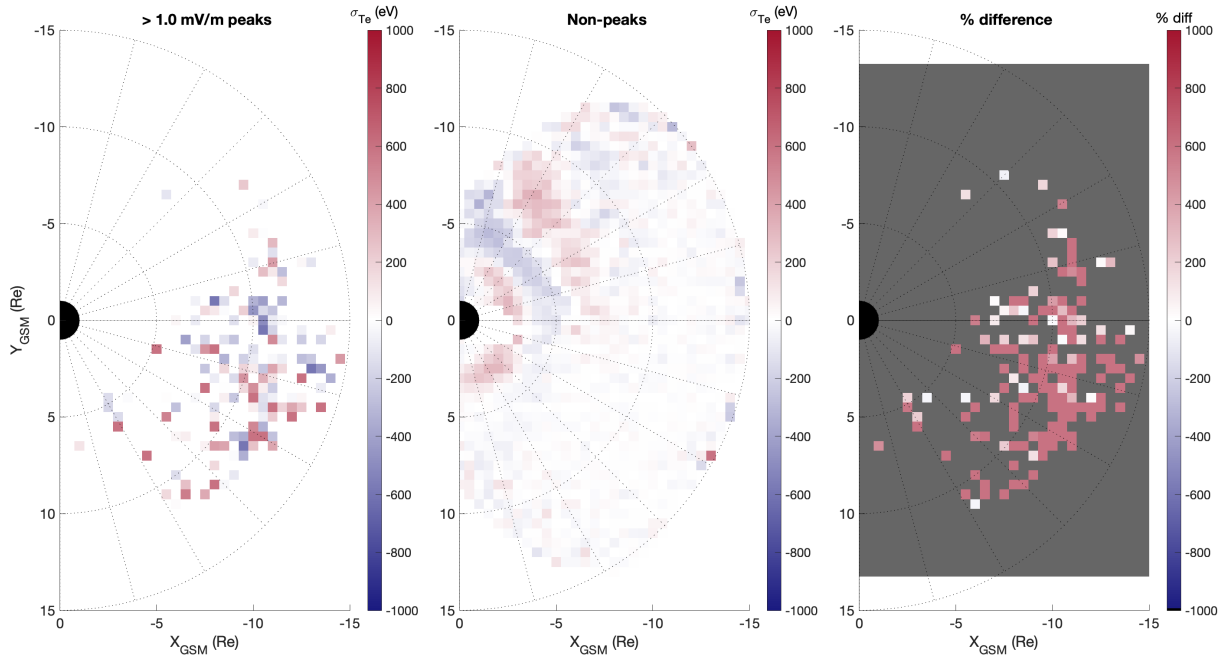

Figure 6. Electron temperature fluctuations for >1 mV/m peaks (left), non-peaks (center) and % difference between the peaks and non-peaks (right).

Similarly, we analyzed variations in the 139 keV electron fluxes. Figures 7 and 8 show flux variations plotted on a logarithmic scale for two electric field RMS thresholds, >0.1 mV/m and >1 mV/m, respectively. The center panels show 139 keV electron flux variations for non-peaks, and the right-hand panels show a percent difference between the peaks and non-peaks, $\frac{log(|\sigma_{flux_{peaks}}|)-log(|\sigma_{flux_{non-peaks}}|)}{log(|\sigma_{flux_{peaks}}|)} \cdot 100\%$.

The flux variations increase towards Earth is both cases, peaks and non-peaks. They maximize in the duskside region for peaks. For non-peaks, enhanced variations are observed in the radiation belt region. The resultant percent difference between peaks and non-peaks is largest in the dusk sector adjacent to the outer radiation belt.

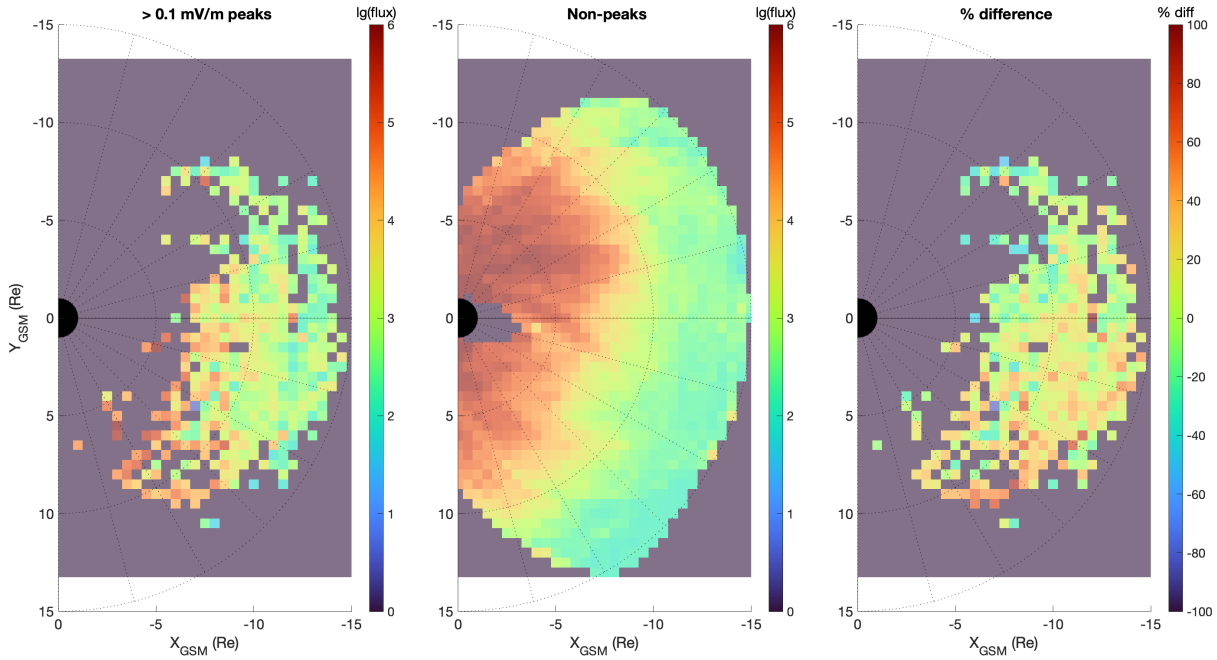

Figure 7. 139 keV electron flux variations for >0.1 mV/m peaks (left), non-peaks (center) and % difference between the lg(flux) for peaks and non-peaks (right).

The higher electric field threshold peaks are associated with more pronounced flux variations that span a larger region in both the azimuthal and radial directions (as

illustrated in Figure 8). The percent difference between peaks and non-peaks is also larger than for >0.1 mV/m electric fields, as observed in the pre-midnight sector.

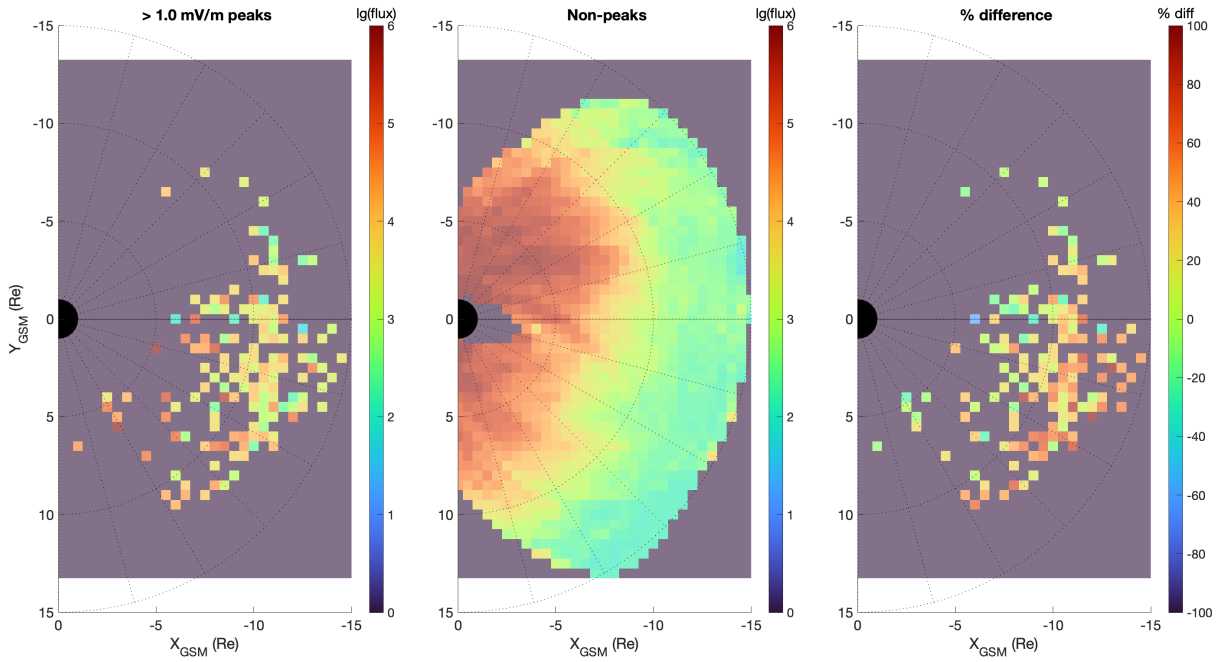

Figure 8. 139 keV electron flux variations for >1 mV/m peaks (left), non-peaks (center) and % difference between the log(flux) for peaks and non-peaks (right).

6. Discussion. The Role of Pre-energized Electron Population in Supplying the Outer Radiation Belt

The potential role of pre-energized electron population in supplying the outer radiation belt is summarized in a schematic in Figure 9. The schematic outlines the scenario where energy is initially being transferred from BBFs to electrons via the large turbulent electric fields. The BBFs are drawn following high-resolution magnetohydrodynamic simulations of BFFs by Wiltberger et al. (2015). The region where electron energization in large amplitude electric fields takes place is based on the analysis presented here. The intense, turbulent electric fields develop primarily in the BBF braking region which extends from ~12 Re to the outer edge of the radiation belts. If an energized tail (>100 keV) in the electron distribution develops from the turbulent electric fields as the data suggest, it is further accelerated as the electrons continue their eastward and inward drift to regions of higher magnetic field strengths. Essentially, the turbulent electric fields create a seed population that can lead to MeV electrons in the radiation belt. A detailed analysis of

297 electron energization and injection by BBFs using electron trajectory tracing in high-
298 resolution magnetohydrodynamic field output from Lyon-Fedder-Mobarry model is
299 presented by Eshetu et al. (2018). They examined the difference between energization
300 of low and high energy electrons and showed that the process is adiabatic for ~<10 keV
301 electrons and non-adiabatic for higher energy electrons. In relation to this study, these
302 results have the following implications. The injection inward of ~10 Re is a combination
303 of grad-B and ExB drift directed towards Earth. As the electrons move inward, the dipole
304 magnetic field starts to dominate such that electrons drift eastward due to grad-B drift.
305 For lower energy core population (~ a few keV), the initial temperature enhancement will
306 be amplified proportionally to the background magnetic field. In a situation where 5 keV
307 electrons propagate from ~10 nT tail magnetic field to geosynchronous orbit where B is
308 ~100 nT, they will get energized by 10 times to 50 keV. The effect will be more
309 pronounced if electron injections propagate down to L~3 (though these events are much
310 rarer) where B is ~1000 nT resulting in ~100 times energization to 500 keV. Electrons,
311 initially energized by turbulent electric fields to ~100 keV (as seen in the SST flux) will
312 also be accelerated by about ten times, to ~MeV if they propagate to the geosynchronous
313 orbit and more if they get farther in, though their motion will no longer be adiabatic, thus
314 not conserving the first adiabatic invariant. Thus, this pre-energized electron population
315 may contribute to a significant fraction of energetic tail of the outer radiat
316

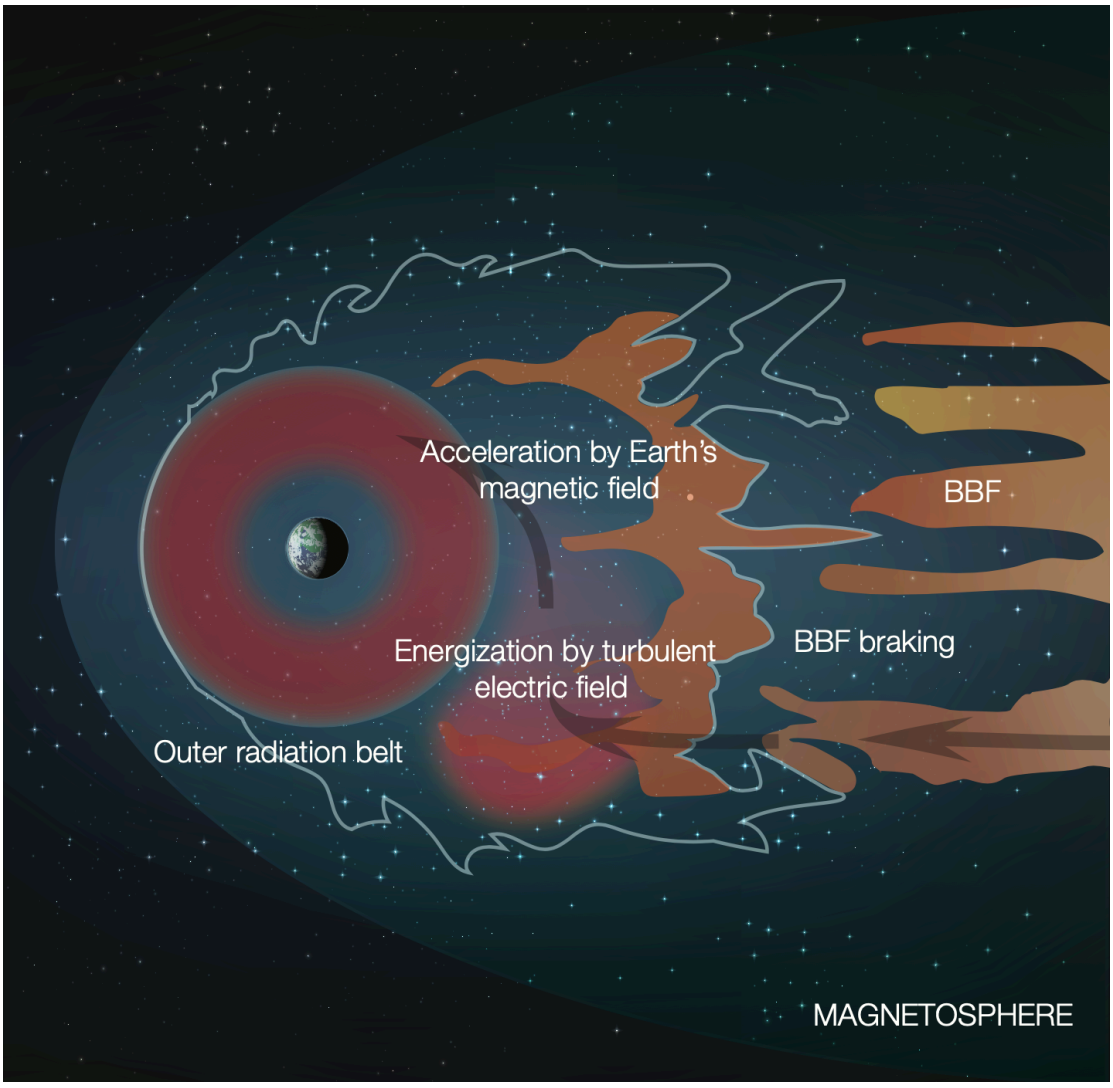

Figure 9. Schematic showing the cascade of energy transfer from BBFs to the outer radiation belt. Based on high-resolution magnetohydrodynamic simulations of BFFs by Wiltberger et al. (2015).

7. Conclusions

High amplitude electric fields in the BBF regions are associated with increases of electron temperature by three times compared to the intervals when they are not observed and cause ten-fold electron temperature fluctuations. They are also associated with variations in energetic energy fluxes in a wide range of energy. There is a clear correlation between the field amplitude and electron temperature and energetic flux variations: stronger fields are related to larger variations, indicative of a local acceleration process. Though these

events are transient and their occurrence is less than 1%, their impact on the magnetospheric dynamics may be rather significant. As the locally pre-energized by an order of magnitude electrons travel toward the inner magnetosphere and get further accelerated by the increasing magnetic field, they supply the high-energy tail of the outer radiation belt.

Acknowledgments

This work was supported by NASA grants for THEMIS mission and funding support from the MMS and Van Allen Probes missions. We acknowledge NASA contract NAS5-02099 and V. Angelopoulos for use of data from the THEMIS Mission. Specifically, J. W. Bonnell and F. S. Mozer for use of EFI data, D. Larson and the late R. P. Lin for use of SST data, C. W. Carlson and J. P. McFadden for use of ESA data, K. H. Glassmeier, U. Auster and W. Baumjohann for the use of FGM data provided under the lead of the Technical University of Braunschweig and with financial support through the German Ministry for Economy and Technology and the German Center for Aviation and Space (DLR) under contract 50 OC 0302.

Data availability

THEMIS data is available at http://themis.ssl.berkeley.edu/data/themis/.

References

El-Alaoui, M., R. L. Richard, M. Ashour-Abdalla, M. L. Goldstein, and R. J. Walker (2013), Dipolarization and turbulence in the plasma sheet during a substorm: THEMIS observations and global MHD simulations, *J. Geophys. Res. Space Physics*, 118, 7752–7761, doi:10.1002/2013JA019322.

Angelopoulos, V., W. Baumjohann, C. F. Kennel, F. V. Coroniti, M. G. Kivelson, R. Pellat, R. J. Walker, H. Lohr, and G. Paschmann (1992), Bursty bulk flows in the inner central plasma sheet, *J. Geophys. Res.*, 97(A4), 4027–4039, doi:10.1029/91JA02701.

Angelopoulos, V., C. F. Kennel, F. V. Coroniti, R. Pellat, M. G. Kivelson, R. J. Walker, C. T. Russel, W. Baumjohann, W. C. Feldman, and J. T. Gosling (1994), Statistical characteristics of bursty bulk flow events, *J. Geophys. Res.*, 99(A11), 21,257–21,280, doi:10.1029/94JA01263.

365 Angelopoulos, V., et al. (1997), Magnetotail flow bursts: Association to global
366 magnetospheric circulation, relationship to ionospheric activity and direct evidence for
367 localization, *Geophys. Res. Lett.*, 24(18), 2271–2274, doi:10.1029/97GL02355.
368
369 Angelopoulos, V. (2008), The THEMIS mission, *Space Sci. Rev.*, 141, 5–34,
370 doi:10.1007/s11214-008-9336-1.
371
372 Angelopoulos, V., Sibeck, D., Carlson, C.W. *et al.* (2008), First Results from the THEMIS
373 Mission. *Space Sci Rev.,* 141**,** 453–476, https://doi.org/10.1007/s11214-008-9378-4.
374
375 Auster, H. U., et al. (2008), The THEMIS fluxgate magnetometer, *Space Sci.*
376 *Rev.*, 141, 235–264, doi:10.1007/s11214-008-9365-9.
377
378 Baumjohann, W., G. Paschmann, and H. Lühr (1990), Characteristics of high-speed ion
379 flows in the plasma sheet, *J. Geophys. Res.*, 95(A4), 3801–3809,
380 doi:10.1029/JA095iA04p03801.
381
382 Bonnell, J. W., F. S. Mozer, G. T. Delory, A. J. Hull, R. E. Ergun, C. M. Cully, V.
383 Angelopoulos, and P. R. Harvey (2008), The Electric Field Instrument (EFI) for
384 THEMIS, *Space Sci. Rev.*, 141, 303–341, doi:10.1007/s11214-008-9469-2.
385
386 Chaston, C. C., J. W. Bonnell, L. Clausen, and V. Angelopoulos (2012), Energy transport
387 by kinetic-scale electromagnetic waves in fast plasma sheet flows, *J. Geophys.*
388 *Res.*, 117, A09202, doi:10.1029/2012JA017863.
389
390 Chaston, C. C., et al. (2014), Observations of kinetic scale field line
391 resonances, *Geophys. Res. Lett.*, 41, 209–215, doi:10.1002/2013GL058507.
392
393 Chen, C. X., and R. A. Wolf (1993), Interpretation of high-speed flows in the plasma
394 sheet, *J. Geophys. Res.*, 98(A12), 21,409–21,419, doi:10.1029/93JA02080.
395
396 Cully, C. M., R. E. Ergun, K. Stevens, A. Nammari, and J. Westfall (2008), The THEMIS
397 digital fields board, *Space Sci. Rev.*, 141, 343–355, doi:10.1007/s11214-008-9417-1.
398
399 Dai, L., J. R. Wygant, C. Cattell, J. Dombeck, S. Thaller, C. Mouikis, A. Balogh, and H.
400 Rème (2011), Cluster observations of surface waves in the ion jets from magnetotail
401 reconnection, *J. Geophys. Res.*, 116, A12227, doi:10.1029/2011JA017004.
402
403 Dai, L., Wang, C., Duan, S., He, Z., Wygant, J. R., Cattell, C. A., Tao, X., Su,
404 Z., Kletzing, C., Baker, D. N., et al. (2015), Near-Earth injection of MeV electrons
405 associated with intense dipolarization electric fields: Van Allen Probes
406 observations, *Geophys. Res. Lett.*, 42, 6170– 6179, doi:10.1002/2015GL064955.
407
408 Delcourt, D. C. (2002). Particle acceleration by inductive electric fields in the inner
409 magnetosphere. *Journal of Atmospheric and Solar - Terrestrial Physics*, 64(5-6), 551–
410 559. 10.1016/S1364-6826(02)00012-3.

Dubyagin, S., Ganushkina, N. Y., Sillanpää, I., and Runov, A. (2016), Solar wind-driven variations of electron plasma sheet densities and temperatures beyond geostationary orbit during storm times, *J. Geophys. Res. Space Physics*, 121, 8343– 8360, doi:10.1002/2016JA022947.

Ergun, R. E., L. Andersson, Y.-J. Su, D. L. Newman, M. V. Goldman, W. Lotko, C. C. Chaston, and C. W. Carlson (2005), Localized parallel electric fields associated with inertial Alfvén waves, *Phys. Plasmas*, 12, 072901.

Ergun, R. E., et al. (2009), Observations of double layers in Earth's plasma sheet, *Phys. Rev. Lett.*, 102, 155002, doi:10.1103/PhysRevLett.102.155002.

Ergun, R. E., Goodrich, K. A., Stawarz, J. E., Andersson, L., and Angelopoulos, V. (2015), Large-amplitude electric fields associated with bursty bulk flow braking in the Earth's plasma sheet. *J. Geophys. Res. Space Physics*, 120, 1832– 1844. doi: 10.1002/2014JA020165.

Ergun, R. E. *et al.* (2020), Particle Acceleration in Strong Turbulence in the Earth's Magnetotail,
ApJ, 898, 153, https://doi.org/10.3847/1538-4357/ab9ab5.

Eshetu, W. W., Lyon, J. G., Hudson, M. K., & Wiltberger, M. J. (2019). Simulations of electron energization and injection by BBFs using high-resolution LFM MHD fields. *Journal of Geophysical Research: Space Physics*, 124, 1222– 1238. https://doi.org/10.1029/2018JA025789.

Gabrielse, C., Angelopoulos, V., Runov, A., and Turner, D. L. (2012), The effects of transient, localized electric fields on equatorial electron acceleration and transport toward the inner magnetosphere, *J. Geophys. Res.*, 117, A10213, doi:10.1029/2012JA017873.

Gabrielse, C., Angelopoulos, V., Runov, A., and Turner, D. L. (2014), Statistical characteristics of particle injections throughout the equatorial magnetotail, *J. Geophys. Res. Space Physics*, 119, 2512– 2535, doi:10.1002/2013JA019638.

Karimabadi, H., et al. (2013), Coherent structures, intermittent turbulence, and dissipation in high-temperature plasmas, *Phys. Plasmas*, 20, 012,303–012,315, doi:10.1063/1.4773205.

Kindel, J. M., and C. F. Kennel (1971), Topside current instabilities, *J. Geophys. Res.*, 76(13), 3055–3078, doi:10.1029/JA076i013p03055.

Liu, J., V. Angelopoulos, A. Runov, and X.-Z. Zhou (2013), On the current sheets surrounding dipolarizing flux bundles in the magnetotail: The case for wedgelets, *J. Geophys. Res. Space Physics*, 118, 2000–2020, doi:10.1002/jgra.50092.

Liu, J., Angelopoulos, V., Zhang, X.-J., Turner, D. L., Gabrielse, C., Runov, A., Li, J., Funsten, H. O., and Spence, H. E. (2016), Dipolarizing flux bundles in the cis-geosynchronous magnetosphere: Relationship between electric fields and energetic particle injections, *J. Geophys. Res. Space Physics*, 121, 1362– 1376, doi:10.1002/2015JA021691.

Lysak, R. L., Y. Song, and T. W. Jones (2009), Propagation of Alfvén waves in the magnetotail during substorms, *Ann. Geophys.*, 27, 2237–2246, doi:10.5194/angeo-27-2237-2009.

Ma, X., Nykyri, K., Dimmock, A., & Chu, C. (2020). Statistical study of solar wind, magnetosheath, and magnetotail plasma and field properties: 12+ years of THEMIS observations and MHD simulations. *Journal of Geophysical Research: Space Physics*, 125, e2020JA028209. https://doi.org/10.1029/2020JA028209.

McFadden, J. P., C. W. Carlson, D. Larson, M. Ludlan, R. Abiad, B. Elliott, P. Turin, M. Marckwordt, and V. Angelopoulos (2008), The THEMIS ESA plasma instrument and in-flight calibration, *Space Sci. Rev.*, 141, 277–302, doi:10.1007/s11214-008-9440-2.

Motoba, T., Ohtani, S., Claudepierre, S.G., Reeves, G.D., Ukhorskiy, A.Y. and Lanzerotti, L.J. (2020), Dynamic Properties of Particle Injections Inside Geosynchronous Orbit: A Multisatellite Case Study. J. Geophys. Res. Space Physics, 125: e2020JA028215. https://doi.org/10.1029/2020JA028215.

Mozer, F. S., S. D. Bale, J. W. Bonnell, C. C. Chaston, I. Roth, and J. Wygant (2013), Megavolt parallel potentials arising from double-layer streams in the Earth's outer radiation belt, *Phys. Rev. Lett.*, 111(23), 235002, doi:10.1103/PhysRevLett.111.235002.

Mozer, F. S., Agapitov, O. V., Artemyev, A., Drake, J. F., Krasnoselskikh, V., Lejosne, S., and Vasko, I. (2015), Time domain structures: What and where they are, what they do, and how they are made. *Geophys. Res. Lett.*, 42, 3627– 3638. doi: 10.1002/2015GL063946.

Nagai, T., I. Shinohara, S. Zenitani, R. Nakamura, T. K. M. Nakamura, M. Fujimoto, Y. Saito, and T. Mukai (2013), Three-dimensional structure of magnetic reconnection in the magnetotail from Geotail observations, *J. Geophys. Res. Space Physics*, 118, 1667–1678, doi:10.1002/jgra.50247.

Nakamura, R., et al. (2014), Low-altitude electron acceleration due to multiple flow bursts in the magnetotail, *Geophys. Res. Lett.*, 41, 777–784, doi:10.1002/2013GL058982.

Newman, D. L., M. V. Goldman, R. E. Ergun, and A. Mangeney (2001), Formation of double layers and electron holes in a current-driven space plasma, *Phys. Rev. Lett.*, 87(25), 255001, doi:10.1103/PhysRevLett.87.255001.

Nishimura, Y., J. Wygant, T. Ono, M. Iizima, A. Kumamoto, D. Brautigam, and F. Rich (2008), Large-amplitude wave electric field in the inner magnetosphere during substorms, *J. Geophys. Res.*, 113, A07202, doi:10.1029/2007JA012833.

Ohtani, S., Shay, M. A., and Mukai, T. (2004), Temporal structure of the fast convective flow in the plasma sheet: Comparison between observations and two-fluid simulations, *J. Geophys. Res.*, 109, A03210, doi:10.1029/2003JA010002.

Raj, A., T. Phan, R. P. Lin, and V. Angelopoulos (2002), Wind survey of high-speed bulk flows and field-aligned beams in the near-Earth plasma sheet, *J. Geophys. Res.*, 107(A12), 1419, doi:10.1029/2001JA007547.

Sigsbee, K., Cattell, C. A., Fairfield, D., Tsuruda, K., and Kokubun, S., (2002), Geotail observations of low-frequency waves and high-speed earthward flows during substorm onsets in the near magnetotail from 10 to 13 R_E, *J. Geophys. Res.*, 107(A7), doi:10.1029/2001JA000166.

Shiokawa, K., W. Baumjohann, and G. Haerendel (1997), Braking of high-speed flows in the near-Earth tail, *Geophys. Res. Lett.*, 24(10), 1179–1182, doi:10.1029/97GL01062.

Sorathia, K. A., Ukhorskiy, A. Y., Merkin, V. G., Fennell, J. F., & Claudepierre, S. G. (2018). Modeling the depletion and recovery of the outer radiation belt during a geomagnetic storm: Combined MHD and test particle simulations. *Journal of Geophysical Research: Space Physics*, 123, 5590– 5609. https://doi.org/10.1029/2018JA025506.

Stawarz, J. E., Ergun, R. E., and Goodrich, K. A. (2015), Generation of high-frequency electric field activity by turbulence in the Earth's magnetotail. *J. Geophys. Res. Space Physics*, 120, 1845– 1866. doi: 10.1002/2014JA020166.

Ukhorskiy, A. Y., Sitnov, M. I., Merkin, V. G., Gkioulidou, M., and Mitchell, D. G. (2017), Ion acceleration at dipolarization fronts in the inner magnetosphere, *J. Geophys. Res. Space Physics*, 122, 3040– 3054, doi:10.1002/2016JA023304.

Ukhorskiy, A. Y., Sorathia, K. A., Merkin, V. G., Sitnov, M. I., Mitchell, D. G., & Gkioulidou, M. (2018). Ion trapping and acceleration at dipolarization fronts: High-resolution MHD and test-particle simulations. *Journal of Geophysical Research: Space Physics*, 123, 5580– 5589. https://doi.org/10.1029/2018JA025370.

Wang, C.-P., Gkioulidou, M., Lyons, L. R., and Angelopoulos, V. (2012), Spatial distributions of the ion to electron temperature ratio in the magnetosheath and plasma sheet, *J. Geophys. Res.*, 117, A08215, doi:10.1029/2012JA017658.

Williams, D. J., D. G. Mitchell, C. Y. Huang, L. A. Frank, and C. T. Russell (1990), Particle acceleration during substorm growth and onset, *Geophys. Res. Lett.*, 17(5), 587–590, doi:10.1029/GL017i005p00587.

548 Wiltberger, M., Merkin, V., Lyon, J. G., and Ohtani, S. (2015), High-resolution global
549 magnetohydrodynamic simulation of bursty bulk flows. *J. Geophys. Res. Space*
550 *Physics*, 120, 4555– 4566. doi: 10.1002/2015JA021080.
551
552 Wygant, J. R., et al. (2002), Evidence for kinetic Alfvén waves and parallel electron
553 energization at 4–6 R_E altitudes in the plasma sheet boundary layer, *J. Geophys.*
554 *Res.*, 107(A8), 1201, doi:10.1029/2001JA900113.